UC Berkeley
UC Berkeley Previously Published Works

Title

Universal optothermal micro/nanoscale rotors.

Permalink

https://escholarship.org/uc/item/3473b360

Journal

Science Advances, 8(24)

Authors

Ding, Hongru

Kollipara, Pavana

Kim, Youngsun

et al.

Publication Date

2022-06-17

DOI

10.1126/sciadv.abn8498

OPTICS

Universal optothermal micro/nanoscale rotors

Hongru Ding[1], Pavana Siddhartha Kollipara[1], Youngsun Kim[2], Abhay Kotnala[1,2], Jingang Li[2], Zhihan Chen[2], Yuebing Zheng[1,2]*

Rotation of micro/nano-objects is important for micro/nanorobotics, three-dimensional imaging, and lab-on-a-chip systems. Optical rotation techniques are especially attractive because of their fuel-free and remote operation. However, current techniques require laser beams with designed intensity profile and polarization or objects with sophisticated shapes or optical birefringence. These requirements make it challenging to use simple optical setups for light-driven rotation of many highly symmetric or isotropic objects, including biological cells. Here, we report a universal approach to the out-of-plane rotation of various objects, including spherically symmetric and isotropic particles, using an arbitrary low-power laser beam. Moreover, the laser beam is positioned away from the objects to reduce optical damage from direct illumination. The rotation mechanism based on opto-thermoelectrical coupling is elucidated by rigorous experiments combined with multiscale simulations. With its general applicability and excellent biocompatibility, our universal light-driven rotation platform is instrumental for various scientific research and engineering applications.

INTRODUCTION

Micro/nanorotors or controlled rotation of micro/nanoscale objects play crucial roles in sensing, imaging, biomedicine, and manufacturing. They have proved effective in the detection of vacuum friction (1), few-nanometer fabrication (2), precise nanosurgery (3), and microfluidic flow control (4). Light-driven micro/nanorotors are promising because of their noncontact fuel-free operation (5, 6). The optical torque that drives a rotor originates from asymmetric absorption and scattering of light by the rotor. The rotation requires precise control of polarization (1, 7–9) and intensity profile of the laser beams (10–12) or sophisticated design of geometry (13, 14) and composition (15–17) of the rotor. The former often relies on complex optics to create designer laser beams that lead to the strong asymmetric light-rotor interactions and thus the large enough optical torques for the rotation (13, 18). Optically induced Marangoni forces were also adopted to rotate microparticles (19, 20). In particular, to rotate homogenous and symmetric particles (21) and live cells (22), multiple-beam optical tweezers were proposed. Moreover, optical torques are reduced substantially when the rotor size decreases (23). The reduced torques make it challenging to precisely control nanorotors, which experience strong Brownian motion in fluids. It has remained challenging for simple and low-power optics to achieve light-driven rotation of a wide range of objects, including optically symmetric synthetic particles and biological cells.

It becomes more challenging to achieve light-driven out-of-plane rotation (i.e., rotation of an object around an axis parallel to the substrate) (24, 25). By enabling three-dimensional (3D) interrogation of objects such as biological particles, out-of-plane rotation techniques would improve rolling cell adhesion measurements (26, 27), single-cell engineering (28), organism identification (29), and microsurgery (30–33). Recently, light-driven out-of-plane rotation has only been realized using multiple-beam optical tweezers (10, 34) or combining light with a microfluidic field (35) or an external electric field (36). In a theoretical paper, Lou et al. (37) proposed the use

of anisotropic optical trapping for out-of-plane rotation based on single-beam optical tweezers, which would require complex optics and high-power laser beams. Intense light with transverse angular momentum may also provide the torque for out-of-plane rotation in theory (38); however, additional forces are required to balance the much larger in-plane forces (radiation pressure and spin force) exerted on the particles, which is extremely challenging in experiments. So far, out-of-plane rotors using a single low-power laser beam have not been achieved.

Here, we propose the concept of opto–thermoelectric (TE) rotation (OTER), which harnesses optothermally generated electrokinetic force, depletion force, and electric force to drive out-of-plane rotation of arbitrary micro/nanoparticles based on simple and low-power optics. We have even achieved the rotation of spherically symmetric and homogenous micro/nanoparticles using a single Gaussian laser beam of linear polarization and ultralow power. In addition, OTER is operated with the laser beam being positioned away from the rotors to reduce the damage caused by direct light illumination. Combining experiments with multiscale simulations, we reveal that the optothermal rotation is realized by the electrokinetic interaction between micro/nanoparticles and the substrate with thermoresponsive surface charge. To show the general applicability of our OTER strategy, we have demonstrated the rotation of objects of diverse sizes (from subwavelength scale to micrometer scale), materials (biological, polymeric, dielectric, and composite colloids), and shapes (aspect ratios ranging from 1 to 8). The rotor behaviors such as rotation rate, rotation axis, and particle-laser (PL) distance can be further tailored on-demand by controlling the incident light and surface chemistry.

RESULTS

Working mechanism of universal light-driven rotors

The experimental setup and working mechanism of OTER are illustrated in Fig. 1. The optothermal forces (TE force, depletion force, and electrokinetic force) exerted on particles are generated by a laser beam heating a functionalized plasmonic substrate immersed in a solution with ions and molecules. The net force and torque can be tailored by the laser power and laser-particle distance to enable the
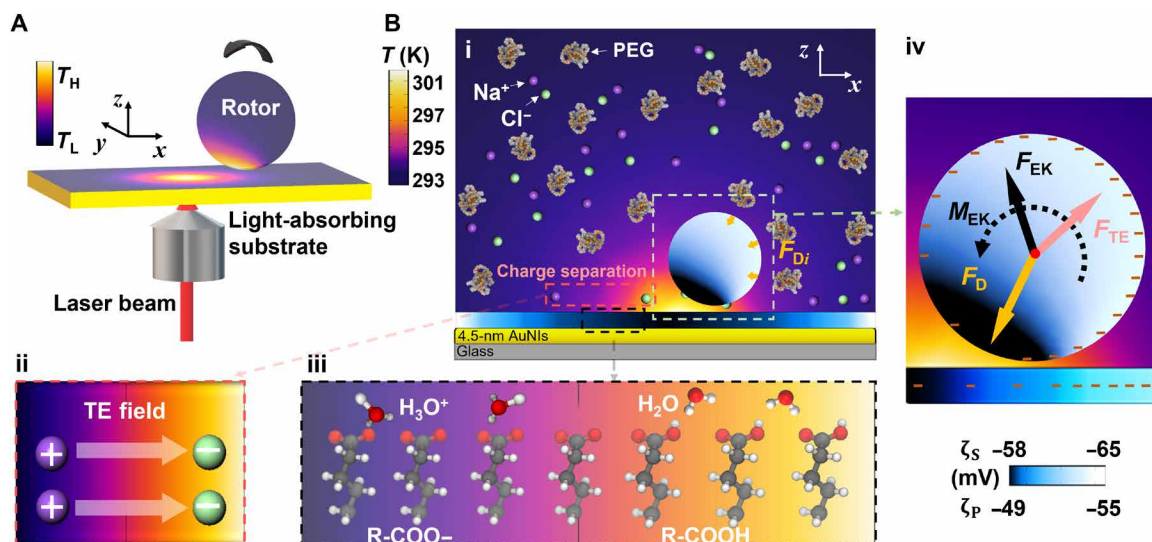
Fig. 1. Working mechanism of light-driven out-of-plane rotation of micro/nanoscale rotors. (**A**) A simplified schematic illustrating the experimental setup and operation for OTER of micro/nanoparticles. (**B**) Working mechanism of OTER: (i) In the nonuniform temperature field, Na^+ and Cl^- ions and PEG molecules diffuse to the cold region. Yellow arrows indicate discrete depletion forces (F_{Di}) acting on the rotor, which lead to a total depletion force (F_D) in (iv). (ii) A TE field is created by the separation Na^+ and Cl^- ions owing to their different thermodiffusion coefficients. Gray arrows indicate the direction of the TE field. (iii) The temperature field also affects the dissociation of carboxylic function groups, thus the surface charges on the substrate. (iv) Optothermal forces and torque on the rotor: In the steady state, the gradient distribution of PEG molecules generates an attractive depletion force (F_D) on the particle. A repulsive force (F_{TE}) is generated from the TE field. A thermo-electrokinetic force (F_{EK}) is from the 11-mercaptoundecanoic acid–coated plasmonic substrate with nonuniform thermo-responsive surface charge (from −65 to −58 mV). The surface charge of most particles also varies with the temperature due to their ionized acid groups on the surface. For instance, the local surface charge of a carboxylic functionalized polystyrene (PS) particle ranges from −55 to −49 mV. The "−" symbols indicate the temperature-dependent distributions of negative charges on the surface of the particle and substrate. The light-irradiated regimes with the higher temperature feature the lower charge density. A net torque, M_{EK}, can be generated on the particle at the certain position where a balance is reached among F_D, F_{TE}, and F_{EK}. The optical power is 78.4 μW. The red dot marks the centroid of the particle.

out-of-plane rotation of micro/nano-objects. Specifically, by directing a laser beam to a light-absorbing substrate (a porous Au film as an example; see Materials and Methods and fig. S1 for details), a tailorable temperature field can be established in a few dozens of microseconds in the aqueous solution containing the rotor, i.e., the sphere in Fig. 1A. To optothermally generate the forces and torque required for the stable rotation of the rotor, we added polyethylene glycol (PEG) molecules and phosphate-buffered saline (PBS) into water and functionalized the substrate with carboxylic acid–terminated alkanethiol self-assembled monolayers (COOH-SAMs) (Fig. 1Bi).

Without optical heating, the particles, ions, and molecules are randomly dispersed in the solution with uniform temperature distribution (see fig. S2). Upon the illumination of the laser beam, a maximum temperature rise of ~9 K was obtained as illustrated in Fig. 1B (see note S1 for measured temperature distribution). The light-generated temperature gradient results in the spatial separation of Na^+ and Cl^- ions (the major ingredients of PBS), creating a TE field (Fig. 1Bii) that drives the thermo-electrophoresis of the charged rotor. We should note that the thermal polarization of water molecules results in an opposite TE field but the direction of the accumulative TE field is dominated by ionic charge separation (*39*). Accordingly, a repulsive TE force (F_{TE}) acts on the negatively charged particle. Meanwhile, the temperature gradient leads to the thermal diffusion of PEG molecules, generating a concentration gradient. As a result, an osmotic pressure–induced attractive depletion force (F_D) (*40*, *41*), which is directed toward the hot region, is acted on the rotor (Fig. 1Bi).

To generate a torque on the particle for rotation, we further exploited the surface charge gradients on the substrate to provide optothermally tunable electrokinetic force (named thermo-electrokinetic

force). In a uniform temperature field, both the particle and substrate have uniform negative surface charges (see note S2 for zeta potential measurements). High temperature generally suppresses the dissociation of acid molecules according to Van't Hoff equation (*42*, *43*). For instance, the carboxylic acid is prone to dissociate into a conjugate base (R-COO$^-$) and a hydrogen ion (H$^+$) in the low-temperature region (Fig. 1Biii). Therefore, the substrate has a surface charge gradient in the nonuniform temperature field, exerting a thermo-electrokinetic force with upward z component and x component toward the hot region on the rotor. The thermo-electrokinetic force can be decomposed into a force (F_{EK}) passing through the centroid of the particle and a torque (M_{EK}) that drives the rotation as shown in Fig. 1Biv. A detailed analysis of the three forces can be found in fig. S3. The balance among the depletion, TE, and thermo-electrokinetic forces passing through the centroid can be attained at a suitable rotor light distance, where the thermo-electrokinetic torque drives a steady rotation of the rotor. The rotation of particles is fundamentally driven by heat, which was generated using a laser beam in our case. While alternative techniques such as Joule heating of a micro/nanostructure fixed on the substrate may also generate similar thermal forces, laser-induced heating is a more convenient strategy as it requires no additional fabrication and enables dynamic manipulation of rotors.

Characterizations and modeling of OTER

To characterize and model the OTER, we start with a 2.8-μm polystyrene (PS) particle with carboxylic functional groups as a rotor. The light-driven rotors allow us to characterize their rotation behavior in situ with optical microscopy. However, under the bright-field

optical microscope, the rotation of the PS microparticle was barely observable, and the rotation rate could not be measured. To facilitate the characterization of the rotation behavior, we labeled the PS microparticle with two fluorescent nanobeads through streptavidin-biotin binding (Fig. 2Ai). Figure 2A(ii to vi) shows the successive fluorescent images demonstrating the out-of-plane rotation of a PS particle driven by a 660-nm laser at the power of 78.4 μW in 5% PEG/5% PBS solution (also see movie S1). The variation in the position of the two nanobeads in the images reveals the orientation change of the PS particle due to the light-driven out-of-plane rotation. A detailed investigation of the rotation direction can be found in fig. S4. The fluorescence intensity of a predefined region encircling the rotor was measured over time for quantitative estimation of the rotation rate (Fig. 2B). The fluorescence signal showed a periodic behavior corresponding to the rotation of the particle at an average rotation rate of 32.0 rpm. Rotation of the particle in 5% PEG/4.5 mM NaCl solution was performed as a control experiment to evaluate the effect of other ions in PBS solution; a similar rotation rate, 29.7 rpm, was obtained. Different from conventional light-driven rotor systems where rotors are directly illuminated by laser beams (44), the opto-TE rotors operate at a certain distance away from the laser beam. Such an off-axis rotation would protect delicate rotors such as live cells from the damage caused by high-power optical illumination. As illustrated in the insets of Fig. 2A (ii to vi), the PL distance is around 2 μm.

To quantitatively analyze the working forces of OTER, we combined experimental measurements with finite element analysis (FEA), molecular dynamics (MD), and finite-difference time-domain (FDTD) simulations (see Materials and Methods and note S3 for simulation details). In the nonuniform temperature field, thermo-responsive charges on the rotor and substrate vary with the rotor location. Therefore, thermo-electrokinetic force acting on the rotor changes with PL distance, so does the torque on the rotor. We calculated the optothermal forces (i.e., depletion force, TE force, and thermo-electrokinetic

force) and torques acted on the rotor as a function of PL distance. Depletion force is given as

$$F_\mathbf{D} = -\oint c_{\text{PEG}} k_\mathrm{B} T \, dA_r \hat{\boldsymbol{n}} \tag{1}$$

where c_{PEG} is the local concentration of PEG molecules, k_B is the Boltzmann constant, T is the local temperature, dA_r is the differential area element on the particle surface, and $\hat{\boldsymbol{n}}$ is a unit vector normal to the rotor surface. TE force was obtained by the integration of parallel components of the TE field at the rotor surface

$$F_{\text{TE}} = \oint \sigma_r E_{\text{TE},\parallel} \, dA_r \tag{2}$$

where σ_r is the surface charge density of the rotor measured from the zeta potential and $E_{\text{TE},\parallel}$ is the tangential component of the TE field along the rotor. Thermo-electrokinetic force is expressed as

$$F_{\text{EK}} = \oint \sigma_r \, dA_r \int_{x \to -\infty}^{x \to \infty} \int_{y \to -\infty}^{y \to \infty} E_\parallel \, dx dy \tag{3}$$

where $E_\parallel$ is the parallel component of the electric field (which is generated by the substrate) on the rotor surface (see note S4).

Please note that we refer to forces passing through the centroid of the rotor when analyzing the forces along the x, y, and z directions (Fig. 1A). Originating from the thermodiffusion of molecules and ions, $F_\mathbf{D}$ and F_{TE} strongly depend on the temperature gradient in the solution (see note S4 for optothermal force analysis) (45). Because the spatial distribution of temperature gradient is not uniform (fig. S5), $F_\mathbf{D}$ and F_{TE} along the x axis vary with PL distance according to Eqs. 1 and 2 (Fig. 3A). As shown in the inset of Fig. 3A, in PEG/PBS solutions, $F_\mathbf{D}^x$ and F_{TE}^x on a negatively charged PS particle have similar magnitude but opposite signs. The x component of the thermo-electrokinetic force, F_{EK}^x, is two orders of magnitude smaller than $F_\mathbf{D}^x$ and F_{TE}^x (see fig. S6A). Therefore, $F_\mathbf{D}^x$ and F_{TE}^x dominate the migration of the PS particle. In the x axis, a force balance
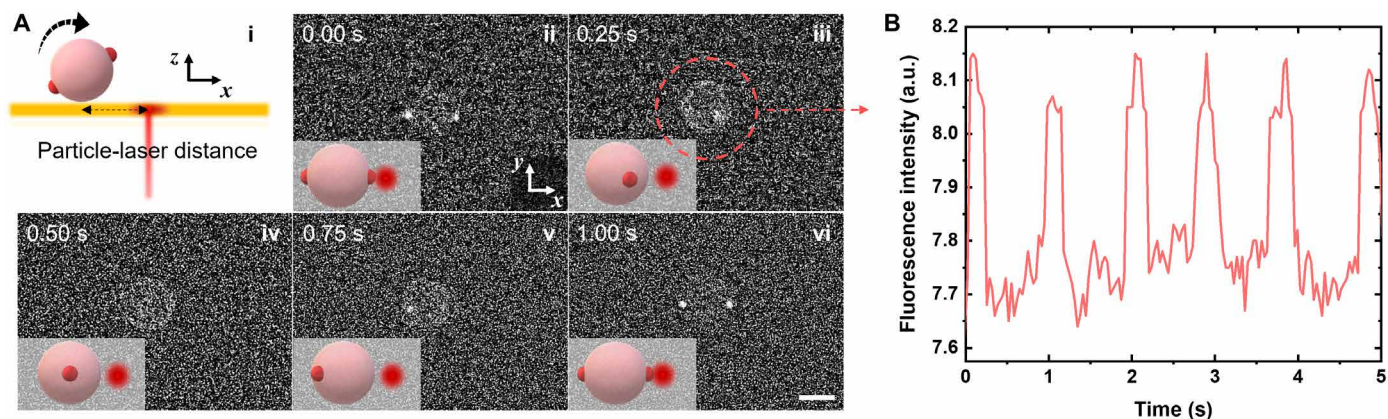

Fig. 2. In situ optical characterization of light-driven out-of-plane rotation of a spherical microparticle. (**A**) (i) Schematic illustration of the out-of-plane rotation of a spherical PS particle (i.e., rotor) around an axis parallel to the substrate. The laser beam, which propagates perpendicular to the substrate, heats the region of the substrate near the particle. The particle is suspended in a 5% PEG/5% PBS solution covering the substrate. The two red beads are fluorescent nanoparticles for the visualization of the orientation change of the rotor under an epifluorescence microscope. The focal plane of the optical microscope is around 1 μm above the substrate. (ii to vi) Successive fluorescence images of a rotating 2.8-μm PS particle. Insets are schematic illustrations of the orientations of the rotor with two fluorescent nanoparticles as markers. Experimentally, two 40-nm (in diameter) fluorescent PS nanoparticles were attached to the rotor through streptavidin-biotin binding. The red point on the right side of the rotor marks the position of the driving laser beam. Scale bar, 2 μm. (**B**) Time-dependent fluorescence intensity measured from the rotor and its surroundings as marked in (iii) of (A). The out-of-plane rotation of the rotor leads to the periodic fluctuation of the fluorescence intensity. The intensity peaks appear when the rotation leads to both fluorescent nanoparticles in the focal plane of the optical microscope. a.u., arbitrary units.

was reached at the PL distance of 2.1 µm, which is consistent with our measured PL distance (see fig. S7). In the y axis, all the corresponding forces are zero, i.e., the net force $F^y = F_D^y = F_{TE}^y = F_E^y = 0$, because the temperature field is symmetric about the xz plane. In the z axis, the net force $F^z = F_D^z + F_{TE}^z + F_{EK}^z$. A net force of zero along the z axis is obtained by the self-adapting gap (which is estimated as 30 nm) between the rotor and substrate. Specifically, the gap affects the depletion force F_D^z and electrokinetic force F_{EK}^z. As shown Fig. 3A (inset), F_D^z pushes the particle toward the substrate, being balanced by the repulsive F_{EK}^z at a suitable gap plus F_{TE}^z. In this way, an overall force balance can be achieved at a certain PL distance, which is defined as critical PL distance. The net torques on the PS particle at different PL distances were also calculated and shown in Fig. 3B. The hydrodynamic torque acting on a spherical particle rotating around an axis parallel to a planar boundary with a small sphere-wall gap is given by (46, 47)

$$M_d = \omega a^3 \upsilon \rho \phi(d);$$

$$\phi(d) = C\left(0.4 \log\left(\frac{a}{a-d}\right) + 0.37\right) \quad (4)$$

where ω is the rotation rate, a is the radius of the particle, υ is the kinematic viscosity of the solution, ρ is the density of the solution, $\phi(d)$ is the correction factor of the wall effect, d is the distance between the rotor and the plane, and C is a constant. For a 2.8-µm PS particle rotating at 35 rpm in the 5% PEG/5% PBS solution, we obtained a simulated thermo-electrokinetic torque of 1.6 pN·nm, which is close to the theoretical hydrodynamic torque, i.e., 1.09 pN·nm (note S5).

A series of control experiments and simulations were conducted to further investigate the roles of electrokinetic force, depletion force, and TE force in the rotor by tailoring the surface charge of the substrate and the components of the solution. First, the role of electrokinetic force was investigated using a bare Au substrate without any coating, on which no rotation was observed. Second, the contribution of depletion force was examined by removing Na$^+$ and Cl$^-$ ions in the solution, where particle trapping was observed. Last, the contribution of TE force was tested by removing PEG molecules in the

solution, where particle repelling was observed. More details can be found in note S6. The electrokinetic force arising from the thermo-responsive surface charge on the light-absorbing substrate functionalized with COOH-SAMs powers the rotation of the rotor, while the depletion and TE forces arising from the thermophoresis of molecules and ions in the PEG/PBS solutions under the light-generated temperature gradient contribute to fixing the rotor in space for a steady rotation. The trapping stiffnesses of rotating microparticles (15.5 pN/µm) and biological cells (13.1 pN/µm) are comparable to optical tweezers as shown in note S7. Thermo-osmosis flow from the substrate is negligible in our rotor because of the highly charged substrate and the thick chamber in which our rotor is located (48–50). In a control experiment, the drift directions and the different drift velocities of PS particles with different zeta potentials further support this assumption (see note S8 for details). Regarding the translational movements of rotors, we do not include thermo-osmotic salt-ion flow around rotors as the contribution of thermo-osmosis to the thermophoresis of rotors is trivial compared to TE effect in electrolyte solutions with large Seebeck coefficients such as PBS used in our case (51–53). The thermal convective drag force is also negligible compared to depletion and TE forces according to our previous work (54).

On-demand control of rotation behaviors

We further studied the effects of solute concentration, laser power, and particle property on the rotation behavior and devised the on-demand control of OTER. To study the roles of PEG molecules in the rotation behaviors of rotors, we measured the rotation rate of a 2.8-µm PS particle in 5% PBS solutions with variable PEG concentrations in the range of 5 to 15%. The amount of PEG molecules does not influence the thermo-electrokinetic force or the torque on the rotor. However, the higher PEG concentration increases the viscosity of the solution (55) and strengthens the depletion force. As a result, the rotation rate at an optical power of 196 µW decreases from 84.1 to 30.9 rpm when PEG concentration increases from 5 to 15% (Fig. 4A). Such a variation in the rotation rate matches well with the theoretically predicted values obtained from Eq. 4 (see note S5 for details). Meanwhile, the critical PL distance shifts from 2.1 to 2.9 µm to reach a new balance between the enhanced depletion
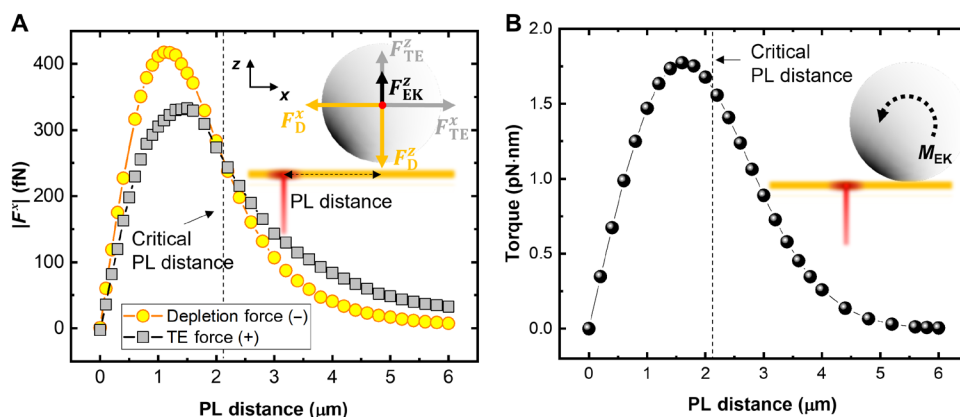

Fig. 3. Quantitative analysis and modeling of OTER of single spherical rotors. (**A**) Simulated magnitudes of depletion force and TE force along the x axis on a 2.8-µm PS particle as a function of PL distance in a 5% PEG/5% PBS solution. As marked by the dashed line, a balance between depletion force and TE force (i.e., zero net force) is reached at a critical PL distance of 2.1 µm. Inset: Schematic illustration of force analysis for the light-driven rotor in the xz plane. The red and white circles represent the laser spot and the rotor, respectively. (**B**) Simulated torque (M_{EK}) acting on the rotor as a function of PL distance. The torque at the critical PL distance (2.1 µm) is around 1.6 pN·nm.

force and the constant TE force. We should note that in a 5% PBS solution with a PEG concentration less than 5%, the 2.8-μm PS particle cannot be fixed; instead, it gets repelled because the repulsive TE force is always larger than the depletion force. That is, the maximum rotation rate in a 5% PBS solution is obtained at the threshold PEG concentration, 5%. To evaluate the dependence of rotation on the PBS concentration, we measured the rotation rate of the PS particle in solutions with the different PBS concentrations, as summarized in Fig. 4B. The surface charge densities of the particle and substrate increase with the PBS concentration according to the Gouy-Chapman theory (*56*). However, the increased ionic strength at the higher PBS concentration enhances the Debye screening effect and reduces the zeta potential of the particle in the solution, which weakens the thermo-electrokinetic force according to Eq. 3. Therefore, the rotation rate decreases when the PBS concentration increases from 5 to 15%. Because of the nonlinear dependence of the charge densities on the ionic strength (*57*), the reduction in rotation rate is larger when the PBS concentration increases from 5 to 10% than that from 10 to 15%. The change in TE force is negligible due to a trade-off between the enhanced TE field and the decreased zeta potential (*39*).

We can also control the rotation behavior by tuning the optical power of the driving laser beam. As shown in Fig. 4B, the rotation

rate increases linearly with optical power. The linear behavior arises from the linear dependence of the temperature gradient and thus the magnitude of thermo-electrokinetic force on the optical power (fig. S6B). However, the maximum rotation rate is limited by a critical optical power beyond which the optical heating of the substrate would generate a vapor bubble (*58*). The bubble generation would lead to a strong Marangoni flow that transports the rotor to the bubble at a velocity of several meters per second, resulting in the printing of the rotor on the substrate (*59, 60*). A maximum rotation rate of 267 rpm was achieved for the 2.8-μm PS particle at an optical power of ~630 μW.

To explore the size effect on the rotation behavior, we measured and simulated rotation rates of spherical particles, along with torques acting on the particles, as a function of the particle size, as shown in Fig. 4C. Approximately, the overall calculated torque, thermo-electrokinetic torque subtracted by optical torque (note S5 and fig. S8), increases linearly with the particle size. It means that the thermo-electrokinetic force parallel to the particle surface ($F_{EK//}$) is almost independent of particle size (see fig. S9A) and the change in thermo-electrokinetic torque mainly arises from the particle's radius. The constant $F_{EK//}$ is the synergy of the enlarged particle surface, the reduced gradient of surface charge on the particle, and varying PL distance. The temperature gradient at the particle center decreases
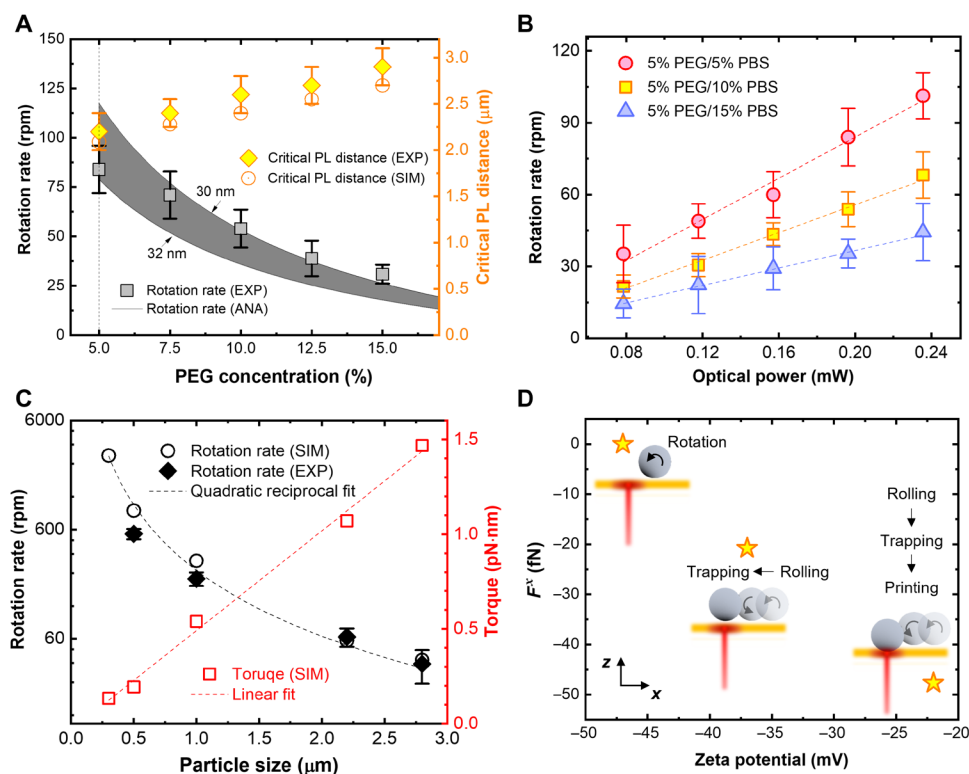

Fig. 4. Parametric study and on-demand control of rotation behaviors. (**A**) Rotation rate and critical PL distance of a 2.8-μm PS particle versus PEG concentration in 5% PBS solutions at an optical power of 196 μW. The gray squares and black line are experimentally measured (indicated as "EXP") and analytic (indicated as "ANA") rotation rates, respectively. The gray region represents the rotation rates calculated as particle-substrate gap of 30 to 32 nm. The yellow diamonds and circles are measured and simulated (indicated as "SIM") critical PL distances, respectively. The dashed line marks the threshold PEG concentration (5%), where the rotation rate reaches a maximum value. (**B**) Measured rotation rate of the PS particle in 5% PEG solutions with different PBS concentrations versus the optical power of laser beam. The dashed lines are linear fittings of the measured values. (**C**) Measured and simulated torque and rotation rate as a function of particle size in a 5% PEG/5% PBS solution. The red dashed line is linear fitting ($M = 0.503a + 0.016$; R^2, 0.993) of the simulated torques. The black dashed line is the quadratic reciprocal fitting ($\omega = 15.9a^{-2}$; R^2, 0.997) of the simulated rotation rate. (**D**) Simulated net forces along the *x* axis of 1-μm PS particles with different zeta potentials of −23, −38, and − 47 mV in a 15% PEG/5% PBS solution, which lead to the different behaviors of the particles as illustrated in the insets. The error bars in (A) and (B) show the deviation in multiple measurements with different particles.

from 10.1 to 1.6 K/μm when the particle size increases from 300 nm to 2.8 μm (see fig. S9A). The decreased temperature gradient is due to the increased distance between the larger particle and the laser beam (i.e., critical PL distance increases from 0.47 to 2.1 μm) as shown in fig. S9 (B to D). We further simulated the rotation rates (black circles) of the particles by substituting the simulated torques into Eq. 4, showing a quadratic reciprocal trend, the simulated torques match well the measured rotation rates (black diamonds).

The zeta potential of rotors can also be used to control the rotational behavior. We studied the light-driven rotation of 1-μm PS particles with different zeta potentials of −23, −38, and − 47 mV (see Materials and Methods for preparation of the particles). As shown in Fig. 4D, a steady rotation was observed for the PS particle with the highest zeta potential (−47 mV). The critical PL distance was ~1 μm. The rotating particle remained stable at its position in the static temperature field powered by laser illumination. However, upon the incidence of the laser beam onto the substrate near the particle, the particle with the zeta potential of −38 mV rolled toward the hot region and got trapped at the center of the laser beam (movie S3). The particle with the weakest zeta potential (−23 mV) underwent a sequence of light-driven events involving rolling, trapping, and printing onto the substrate (also see movie S4). The realization of particle rotation, trapping, and printing on a single platform could open new horizons in the fields of micro/nanorobots (*61*), drug delivery (*62*), and micro/nanofabrication (*63*). Figure 4D also shows the calculated net forces on the particles along the *x* axis. For all the calculations in the figure, the PL distance was set at 1 μm. The net force decreases from 0 to −47.7 fN when the zeta potential of the particle increases. The negative net forces stem from the increased attractive depletion force and the decreased repulsive TE force acting on the particles with weak zeta potentials (fig. S9D).

General applicability of OTER

We have demonstrated the general applicability of OTER to biological cells and synthetic particles of diverse materials, sizes, and shapes. Figure 5A displays the time-lapsed fluorescence images, showing the out-of-plane rotation of a 1-μm PS spherical particle labeled by two fluorescent nanobeads (also see movie S5). The rotation rate was measured as 66.6 rpm at an optical power of 15.7 μW. Rotation of a 500-nm PS/Au Janus particle (see Materials and Methods for the particle preparation) with a rate of 163.8 rpm in a 15% PEG/5% PBS solution was demonstrated at the optical power of 9.4 μW (Fig. 5B and movie S6).

When the rotors become smaller, it becomes challenging to visualize their rotation with conventional optical microscopy. To demonstrate the rotation of a 300-nm PS/Au Janus particle, we used dark-field optical microscopy to monitor the variation in the scattered light from the rotating Janus particle (Fig. 5C and movie S7). To further quantify the rotation, we extracted the real-time red-green-blue (RGB) signals from the scattered light of the particle. As shown in Fig. 5D, the magnitude of green and red signals varied periodically with a period of ~0.17 s. The variations in the RGB signals correspond to the orientation change of the Janus particle due to the light-driven rotation (fig. S10). From Fig. 5D, we calculated the rotation rate of the Janus nanoparticle as ~353 rpm.

OTER is also applicable to live cells (Fig. 5, E and F). Because of a large amount of ionized carboxyl and phosphoric acid groups on their surfaces, yeast cells have a high negative zeta potential (*64*). As shown in Fig. 5E, a yeast cell rotated at a high rate of ~300 rpm at an

optical power of 78.5 μW (also see movie S8). Besides the spherical particles, rotation of quasi-1D *Bacillus subtilis* with a high aspect ratio of 8 has also been achieved (Fig. 5F). Because of the much smaller cross section (~0.25 μm in diameter) of *B. subtilis*, the thermo-electrokinetic force on *B. subtilis* is weaker than that on yeast cells. As a result, the rotation rate of *B. subtilis* was around 1 of 10 of the rate of the yeast cell (see movie S9). Beyond fungi and bacteria, OTER shows excellent biocompatibility (see fig. S11) and should also work for the rotation of human cells in most cell culture medium containing ions and nonpolar molecules as long as the balance between depletion force and TE force can be achieved by tuning PEG concentration.

Moreover, OTER is applicable to rotors with more complex architectures. As an example, we demonstrated the out-of-plane rotation of particle dimers, trimers, and hexamers. Figure 5G is the successive optical images showing the real-time rotation of a dimer composed of two 2-μm silica particles (see movie S10). The rotation of a trimer composed of three 1-μm PS particles and a hexamer composed of six 2-μm silica particles are shown in Fig. 5H (also see movie S11) and fig. S12 (also see movie S12), respectively. Note that OTER enables accurate control of the rotation angle, rotation axis, and, thus, rotor orientation by controlling the power, duration, and position of the driving laser beam, facilitating its application in 3D profiling of biological cells and synthetic particles with high-resolution and time-consuming imaging techniques. As shown in Fig. 5G, the long axis of the silica dimer remained perpendicular to the substrate when the laser beam was turned off after the dimer rotation for 1 s. We also demonstrated the precise rotation of a yeast cell along specific rotation axes for targeted angular degrees to reach any desired orientations (see fig. S13 and movie S13). The achievable resolution of rotation on the current platform is ~16°, and the resolution can be further improved with an advanced laser control device (see note S9 and movie S14).

DISCUSSION

By harnessing thermodiffusion of ions and molecules in solutions and thermo-responsive charge at solid/liquid interfaces under the light-generated temperature gradient, we have developed OTER of arbitrary micro/nanoscale objects in a liquid environment with simple and low-power optics. In contrast to previously demonstrated rotors that required laser beams with designed intensity profile and polarization or rotors with sophisticated shapes or material birefringence, OTER enables the out-of-plane rotation of spherically symmetric and isotropic particles along specific rotation axes for targeted angular degrees using a simple, low-power, and linearly polarized Gaussian laser beam. As a general platform, OTER is applicable to diverse biological cells and synthetic particles of variable compositions, sizes, and shapes. On-demand control of the rotation behaviors can be achieved by tuning the solutes or laser beam. Different from the conventional on-axis high-power (5 to 50 mW) rotors systems (*44*), OTER enables off-axis rotation with a low-power (down to 9.4 μW) laser beam, holding great promise for a noninvasive 3D cellular analysis.

We anticipate that with its superior performance compared to conventional rotor platforms in terms of optical power and out-of-plane rotation, universal applicability, and simple optics, OTER will find a wide range of applications in imaging, sensing, and biomedicine. Evanescent waves have largely improved the detection limit of a myriad of imaging and sensing techniques (*65*–*67*) such as total internal
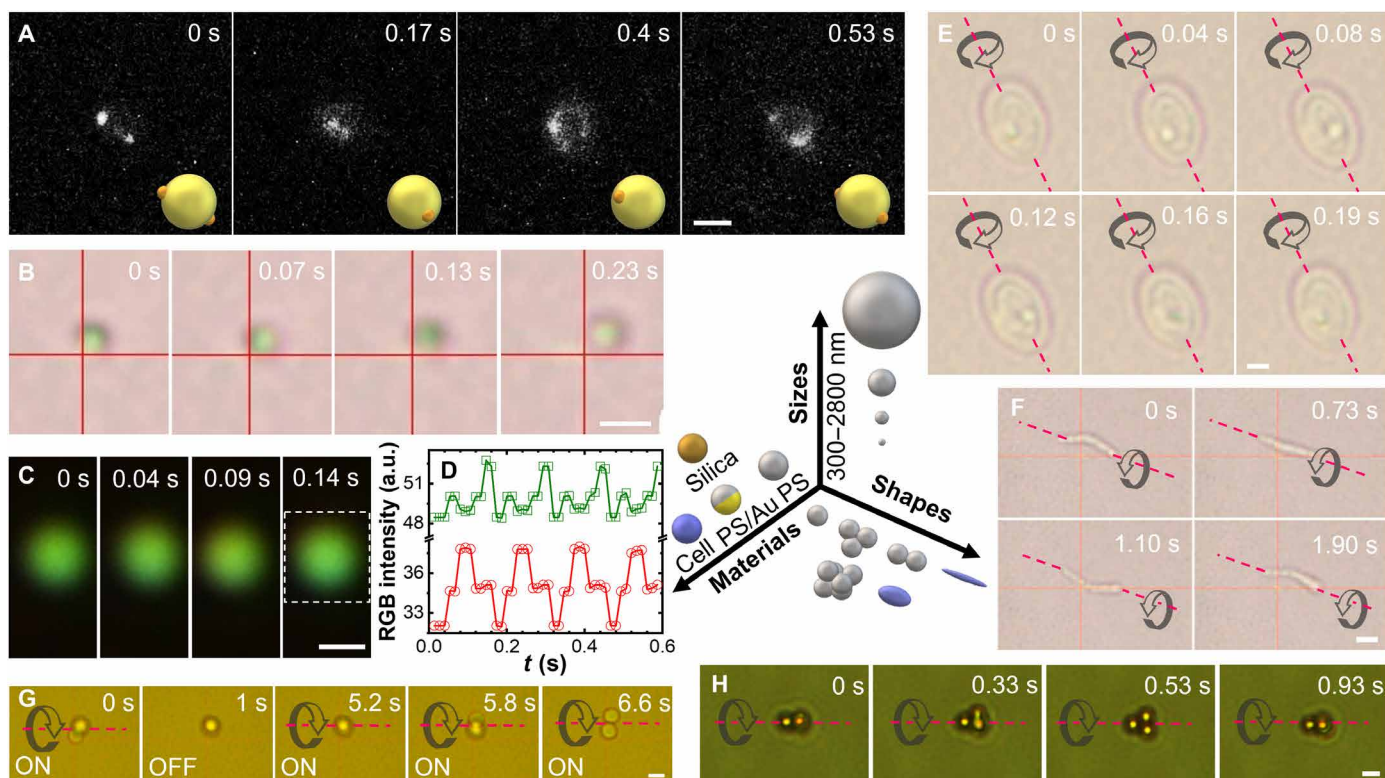
Fig. 5. General applicability of OTER to a variety of rotors with diverse shapes, sizes, and materials. (**A**) Successive fluorescence images of a rotating 1-μm PS particle labeled by fluorescent nanoparticles for the rotation visualization. (**B**) Successive optical images of a rotating 500-nm PS/Au Janus particle. (**C**) Successive dark-field optical images of a rotating 300-nm PS/Au Janus particle. (**D**) Real-time RGB intensity of the dark-field optical images of the Janus particle. The white dash rectangle in (C) marks the selected area from which the RGB intensity is recorded. (**E**) Successive optical images of a rotating yeast cell. (**F**) Successive optical images of a rotating *B. subtilis*. (**G**) Successive optical images of a rotating dimer composed of two 2-μm silica particles. "ON" and "OFF" indicate that the laser beam is turned on and off, respectively. (**H**) Successive optical images of a rotating trimer composed of three 1-μm PS particles. The dash lines and black arrows represent the rotation axes and directions, respectively. Scale bars, 1 μm (A, B, E, F, and H), 500 nm (C), and 2 μm (G). Solutions, 15% PEG/5% PBS (A to C, G, and H) and 5% PEG/5% PBS (E and F).

reflection fluorescence (TIRF) microscopy (*68*); however, it is fundamentally challenging to detect and analyze the top region of a micro-object due to the exponential decay of evanescent waves from a surface. The capability to completely map a sample is crucial because most biological samples are asymmetric and the biomolecules on their surface are nonuniformly distributed. Our technique could overcome the challenge by introducing a simple laser beam to the optical microscopy to rotate the sample on demand, enabling new studies such as vesicle trafficking (*69*) by offering 3D TIRF characterizations. In terms of biomedicine, OTER provides a promising solution to overcome the bottleneck of techniques for measuring receptor-ligand interactions. The adhesion of a receptor to a ligand on cellular surfaces mediate cell-cell and cell-environment communications. Although a variety of assays can measure the affinity of receptor-ligand pairs on the cell surfaces, it is challenging to obtain the affinity of receptors on a rotating cell, which is highly relevant to many biological events. With the capability to rotate diverse single cells, OTER paves a new way toward rolling adhesion assay, contributing to the study of cancer metastasis (*70*) and inflammatory responses (*71*).

While our optothermal rotation overcomes some of the challenges discussed above, we acknowledge the potential limitations of this platform. This optothermal approach requires the use of a light-absorbing substrate, which could restrict its in vivo applications

(*72*). We expect that the platform would play a major role in in vitro biological study where one can rotate cells and synthetic particles in native biofluids (e.g., plasma) containing ions and biomolecules required to generate electric fields and unbalanced osmotic pressure for the optothermal rotation. In addition, the current thermoplasmonic substrate has limited photothermal conversion efficiency in the near-infrared (NIR) range, which may prevent the rotation of larger biological objects (>50 μm) using NIR light. This limitation can be resolved using optothermal substrates with the higher NIR photothermal efficiency, such as hyperbranched Au plasmonic substrate (*73*).

MATERIALS AND METHODS
Materials
PEG 20000, PBS solution, and 11-mercaptohexanoic acid were purchased from Sigma-Aldrich. PS microparticles (2.8, 2.2, 1, and 0.5 μm) with streptavidin ligands, 40-nm yellow-green fluorescent (505/515) nanobeads with biotin ligands, and 2-μm silica particles were purchased from Thermo Fisher Scientific. PS particles (500 and 300 nm) were purchased from Bangs Laboratories.

Substrate preparation
The plasmonic substrates were fabricated by a three-step process. Au films (4.5 nm) were thermally deposited on glass slides at a base

pressure of 8×10^{-6} torr. Then, the Au films were annealed at 550°C for 2 hours. Last, the substrates were immersed in 1 mM 11-mercaptohexanoic acid (solvent:ethanol) at room temperature for 24 hours, followed by rinsing with deionized (DI) water and drying under a nitrogen stream. The porous Au substrate was used for three reasons. First, Au nanoparticle is an efficient light-to-heat conversion agent. Second, the porous structure supports high temperature gradients through heat localization. Last, self-assembly of 11-mercaptohexanoic acid molecules on the Au substrate through Au—S bond has been well established.

Janus particle preparation

PS nanoparticles diluted in DI water were spin-coated on a glass slide to form a monolayer of nanoparticles. A layer of Au film with a thickness of 15 nm was thermally deposited (8×10^{-6} torr) on the monolayer of particles to create the Janus particles. The Janus nanoparticles were detached from the glass and redispersed in PEG/PBS solutions.

Fluorescent labeling

PS particles (2.8 and 1 μm) were diluted with 5% PBS solution by 1000 times. Fluorescent nanobead solution (1 μl) was added into 1 ml of the PS particle solution. The mixed solution was stored at 4°C for 12 hours, followed by centrifugation at 8000 rpm for 5 min at room temperature. The particles were redispersed into PEG/PBS solutions. For 1-μm PS particles with zeta potentials of −38 and −23 mV, the concentrations of PBS solutions for incubation are 10 and 50%, respectively.

FEA simulations

We used a FEA software (COMSOL Multiphysics version 5.4a) to simulate the temperature distribution and electrical potential. Laser heating was modeled as heat influx with a Gaussian laser beam profile with laser power, beam width, and absorptivity as the inputs to define a Gaussian heating source at the bottom edge of the simulation domain. A particle on a substrate was introduced, with varying positions from the laser beam axis. The temperature on the substrate and on the particle surface was obtained as discreet dataset from COMSOL. The differential element of thermo-electrokinetic force was evaluated in MATLAB (version 2020). Modeling details are shown in note S3 including the modeling framework, governing equations, and boundary conditions.

MD simulations

We performed MD simulations for Soret coefficients using the LAMMPS package with a time step of 1 fs at 300 K and ambient pressure. The Soret coefficient can be written as $S_T = -1/x(dx/dT)$, where x is the molar fraction of solute and T is temperature. The spatial distributions of Na and Cl atoms were recorded to obtained x. Thermal velocities were recorded to calculate T. The calculated $S_T(\text{Na}^+)$ and $S_T(\text{Cl}^-)$ in a NaCl solution at the concentration of 15 mM are 3.44×10^{-3} and 1.10×10^{-3} 1/K, respectively. The dimension of simulation box is 3.4 nm by 5.2 nm by 25.9 nm. Periodic boundary conditions were applied in all directions. The rigid SPC/E model (74) was used for water molecules. Widely used TIP4P model (75) was also tested. All-atom optimized potentials for liquid simulation force field (76, 77) were used in all simulations. The long-range electrostatic forces were computed with the P^{3}M method. Lorentz-Berthelot mixing rule was applied for all pairwise Lennard-Jones terms. The cutoff distance in the LJ potential was set to 2.5 σ. Nonequilibrium MD (200 ns) simulations in the canonical ensemble were used to record simulation data after the structure relaxation in the isothermal-isobaric (NPT) ensemble, followed by 1-ns microcanonical (NVE) ensemble. Langevin thermostats were coupled with water molecules in the middle and boundaries of the system to generate temperature gradients. To obtain meaningful statistics, for each set of parameters, eight independent simulations were performed.

FDTD simulation

We used FDTD method (Lumerical Inc.) to calculate optical forces and torques. The refractive indices of the PS particles, glass substrate, and the solution were set as 1.58, 1.52, and 1.34 (78), respectively. To model the plasmonic substrate (porous Au film), a scanning electron microscopy image of the film was imported into the model (see fig. S1). We scaled the image appropriately for an accurate modeling of nanoparticles sizes and spacing. The permittivity of the Au films was taken from (79). The optical forces and torques were calculated through the Maxwell stress tensor at an excitation wavelength of 660 nm. A Gaussian laser beam was used as the excitation source and launched from the glass substrate side. The boundary conditions for all directions were set as perfectly matched layers. The mesh size in the simulation was set as 5 nm.

Optical setup

A 660-nm laser beam (Laser Quantum, Ventus) and a 532-nm laser beam (Coherent, Genesis MX STM-1 W) were expanded with a 5× beam expander (Thorlabs, GBE05-A) and directed to a Nikon inverted microscope (Nikon Ti-E) with a 100× oil objective (Nikon; numerical aperture, 0.5 to 1.3) for the rotor experiments inside a microfluidic chamber of ~120 μm thickness. For the dark-field optical imaging, an air condenser (Nikon, C-AA Achromat/Aplanat Condenser) was used to focus the incident white light onto the sample from the top. A complementary metal oxide–semiconductor camera (Nikon, DS-Fi3) was used to record the optical images. A Notch filter (533 or 658 nm) was placed between the objective and the camera to block the incident laser beam. White light was directed from the top of the stage for bright-field imaging. A halogen lamp was applied through the objective with a green fluorescent protein filter cube (457 to 487/502 to 538 nm for excitation/emission) for fluorescence imaging. The notch filter was removed in fluorescence imaging.

Fluorescent intensity and RGB signal analysis

The fluorescence and dark-field scattering images of the particles were extracted from the recorded videos of the rotating particles. A region of interest encircling the whole particle was defined to record the periodic variation in the average fluorescence intensity and RGB intensity arising from the change in fluorescence and scattering signals from the particle due to its rotation. The periodic signal change was used to estimate the rotation rate of the particle. Each frame is decomposed into RGB channels, and the average values in each channel are plotted as a function of frame number (or time). A dip in the green channel correlates well with a peak in the red channel, which indicates the rotation of the particle.

SUPPLEMENTARY MATERIALS

REFERENCES AND NOTES

1. J. Ahn, Z. Xu, J. Bang, P. Ju, X. Gao, T. Li, Ultrasensitive torque detection with an optically levitated nanorotor. *Nat. Nanotechnol.* **15**, 89–93 (2020).

2. R. K. Soong, G. D. Bachand, H. P. Neves, A. G. Olkhovets, H. G. Craighead, C. D. Montemagno, Powering an inorganic nanodevice with a biomolecular motor. *Science* **290**, 1555–1558 (2000).

3. B. J. Nelson, I. K. Kaliakatsos, J. J. Abbott, Microrobots for minimally invasive medicine. *Annu. Rev. Biomed. Eng.* **12**, 55–85 (2010).

4. U. G. Butaite, G. M. Gibson, Y.-L. D. Ho, M. Taverne, J. M. Taylor, D. B. Phillips, Indirect optical trapping using light driven micro-rotors for reconfigurable hydrodynamic manipulation. *Nat. Commun.* **10**, 1215 (2019).

5. D. G. Grier, A revolution in optical manipulation. *Nature* **424**, 810–816 (2003).

6. B. Qian, D. Montiel, A. Bregulla, F. Cichos, H. Yang, Harnessing thermal fluctuations for purposeful activities: The manipulation of single micro-swimmers by adaptive photon nudging. *Chem. Sci.* **4**, 1420–1429 (2013).

7. J. Ahn, Z. Xu, J. Bang, Y. H. Deng, T. M. Hoang, Q. Han, R. M. Ma, T. Li, Optically levitated nanodumbbell torsion balance and GHz nanomechanical rotor. *Phys. Rev. Lett.* **121**, 033603 (2018).

8. M. Tamura, T. Omatsu, S. Tokonami, T. Iida, Interparticle-interaction-mediated anomalous acceleration of nanoparticles under light-field with coupled orbital and spin angular momentum. *Nano Lett.* **19**, 4873–4878 (2019).

9. M. G. Donato, O. Brzobohatý, S. H. Simpson, A. Irrera, A. A. Leonardi, M. J. Lo Faro, V. Svak, O. M. Maragò, P. Zemánek, Optical trapping, optical binding, and rotational dynamics of silicon nanowires in counter-propagating beams. *Nano Lett.* **19**, 342–352 (2019).

10. M. Kreysing, D. Ott, M. J. Schmidberger, O. Otto, M. Schürmann, E. Martín-Badosa, G. Whyte, J. Guck, Dynamic operation of optical fibres beyond the single-mode regime facilitates the orientation of biological cells. *Nat. Commun.* **5**, 5481 (2014).

11. A. Forrester, J. Courtial, M. J. Padgett, Performance of a rotating aperture for spinning and orienting objects in optical tweezers. *J. Mod. Opt.* **50**, 1533–1538 (2003).

12. L. Paterson, M. P. MacDonald, J. Arlt, W. Sibbett, P. E. Bryant, K. Dholakia, Controlled rotation of optically trapped microscopic particles. *Science* **292**, 912–914 (2001).

13. L. Shao, Z. J. Yang, D. Andren, P. Johansson, M. Kall, Gold nanorod rotary motors driven by resonant light scattering. *ACS Nano* **9**, 12542–12551 (2015).

14. M. Padgett, R. Bowman, Tweezers with a twist. *Nat. Photonics* **5**, 343–348 (2011).

15. F. Han, J. A. Parker, Y. Yifat, C. Peterson, S. K. Gray, N. F. Scherer, Z. Yan, Crossover from positive to negative optical torque in mesoscale optical matter. *Nat. Commun.* **9**, 4897 (2018).

16. R. Reimann, M. Doderer, E. Hebestreit, R. Diehl, M. Frimmer, D. Windey, F. Tebbenjohanns, L. Novotny, GHz rotation of an optically trapped nanoparticle in vacuum. *Phys. Rev. Lett.* **121**, 033602 (2018).

17. Y. Zong, J. Liu, R. Liu, H. Guo, M. Yang, Z. Li, K. Chen, An optically driven bistable Janus rotor with patterned metal coatings. *ACS Nano* **9**, 10844–10851 (2015).

18. F. Nan, Z. Yan, Synergy of intensity, phase, and polarization enables versatile optical nanomanipulation. *Nano Lett.* **20**, 2778–2783 (2020).

19. H. Kim, S. Sundaram, J. H. Kang, N. Tanjeem, T. Emrick, R. C. Hayward, Coupled oscillation and spinning of photothermal particles in Marangoni optical traps. *Proc. Natl. Acad. Sci. U.S.A.* **118**, e2024581118 (2021).

20. S. Nagelberg, J. F. Totz, M. Mittasch, V. Sresht, L. Zeininger, T. M. Swager, M. Kreysing, M. Kolle, Actuation of Janus emulsion droplets via optothermally induced marangoni forces. *Phys. Rev. Lett.* **127**, 144503 (2021).

21. T. Asavei, T. A. Nieminen, V. L. Y. Loke, A. B. Stilgoe, R. Bowman, D. Preece, M. J. Padgett, N. R. Heckenberg, H. Rubinsztein-Dunlop, Optically trapped and driven paddle-wheel. *New J. Phys.* **15**, 063016 (2013).

22. G. Vizsnyiczai, A. Búzás, B. Lakshmanrao Aekbote, T. Fekete, I. Grexa, P. Ormos, L. Kelemen, Multiview microscopy of single cells through microstructure-based indirect optical manipulation. *Biomed. Opt. Express* **11**, 945–962 (2020).

23. A. Ashkin, J. M. Dziedzic, J. E. Bjorkholm, S. Chu, Observation of a single-beam gradient force optical trap for dielectric particles. *Opt. Lett.* **11**, 288–290 (1986).

24. M. Habaza, M. Kirschbaum, C. Guernth-Marschner, G. Dardikman, I. Barnea, R. Korenstein, C. Duschl, N. T. Shaked, Rapid 3D refractive-index imaging of live cells in suspension without labeling using dielectrophoretic cell rotation. *Adv. Sci.* **4**, 1600205 (2017).

25. L. Huang, P. Zhao, F. Liang, W. Wang, Single-cell 3D electro-rotation. *Methods Cell Biol.* **148**, 97–116 (2018).

26. A. B. Yasunaga, I. T. S. Li, Quantification of fast molecular adhesion by fluorescence footprinting. *Sci. Adv.* **7**, (2021).

27. I. T. S. Li, T. Ha, Y. R. Chemla, Mapping cell surface adhesion by rotation tracking and adhesion footprinting. *Sci. Rep.* **7**, 44502 (2017).

28. X. Ding, S. C. S. Lin, B. Kiraly, H. Yue, S. Li, I. K. Chiang, J. Shi, S. J. Benkovic, T. J. Huang, On-chip manipulation of single microparticles, cells, and organisms using surface acoustic waves. *Proc. Natl. Acad. Sci. U.S.A.* **109**, 11105–11109 (2012).

29. D. Ahmed, A. Ozcelik, N. Bojanala, N. Nama, A. Upadhyay, Y. Chen, W. Hanna-Rose, T. J. Huang, Rotational manipulation of single cells and organisms using acoustic waves. *Nat. Commun.* **7**, 11085 (2016).

30. S. Jeon, S. Kim, S. Ha, S. Lee, E. Kim, S. Y. Kim, S. H. Park, J. H. Jeon, S. W. Kim, C. Moon, B. J. Nelson, J.-Y. Kim, S.-W. Yu, H. Choi, Magnetically actuated microrobots as a platform for stem cell transplantation. *Sci. Robot.* **4**, eaav4317 (2019).

31. Y. Alapan, U. Bozuyuk, P. Erkoc, A. C. Karacakol, M. Sitti, Multifunctional surface microrollers for targeted cargo delivery in physiological blood flow. *Sci. Robot.* **5**, eaba5726 (2020).

32. U. Bozuyuk, E. Suadiye, A. Aghakhani, N. O. Dogan, J. Lazovic, M. E. Tiryaki, M. Schneider, A. C. Karacakol, S. O. Demir, G. Richter, M. Sitti, High-performance magnetic FePt (L1$_0$) surface microrollers towards medical imaging-guided endovascular delivery applications. *Adv. Funct. Mater.* **32**, 2109741 (2022).

33. D. Ahmed, T. Baasch, N. Blondel, N. Läubli, J. Dual, B. J. Nelson, Neutrophil-inspired propulsion in a combined acoustic and magnetic field. *Nat. Commun.* **8**, 770 (2017).

34. I. Shishkin, H. Markovich, Y. Roichman, P. Ginzburg, Auxiliary optomechanical tools for 3D cell manipulation. *Micromachines* **11**, 90 (2020).

35. T. Kolb, S. Albert, M. Haug, G. Whyte, Optofluidic rotation of living cells for single-cell tomography. *J. Biophotonics* **8**, 239–246 (2015).

36. W. Liang, X. Yang, J. Wang, Y. Wang, H. Zhang, W. Yang, L. Liu, Label-free characterization of different kinds of cells using optoelectrokinetic-based microfluidics. *Opt. Lett.* **45**, 2454–2457 (2020).

37. X. Lou, N. Yu, R. Liu, K. Chen, M. Yang, Dynamics of a colloidal particle near a thermoosmotic wall under illumination. *Soft Matter* **14**, 1319–1326 (2018).

38. A. Aiello, P. Banzer, M. Neugebauer, G. Leuchs, From transverse angular momentum to photonic wheels. *Nat. Photonics* **9**, 789–795 (2015).

39. H. Ding, P. S. Kollipara, L. Lin, Y. Zheng, Atomistic modeling and rational design of optothermal tweezers for targeted applications. *Nano Res.* **14**, 295–303 (2021).

40. H. R. Jiang, H. Wada, N. Yoshinaga, M. Sano, Manipulation of colloids by a nonequilibrium depletion force in a temperature gradient. *Phys. Rev. Lett.* **102**, 208301 (2009).

41. Y. T. Maeda, A. Tlusty, A. Libchaber, Effects of long DNA folding and small RNA stem-loop in thermophoresis. *Proc. Natl. Acad. Sci. U.S.A.* **109**, 17972–17977 (2012).

42. P. Atkins, J. de Paula, *Physical Chemistry* (Oxford Univ. Press, ed. 8, 2006).

43. M. J. Blandamer, J. Burgess, P. P. Duce, R. E. Robertson, J. W. M. Scott, Analysis of the dependence on temperature of the acid dissociation constants for mono-carboxylic acids in water in terms of a two-stage mechanism. *J. Chem. Soc., Faraday Trans. 1* **77**, 2281–2286 (1981).

44. L. Shao, M. Käll, Light-driven rotation of plasmonic nanomotors. *Adv. Funct. Mater.* **28**, 1706272 (2018).

45. P. S. Kollipara, L. Lin, Y. Zheng, Thermo-electro-mechanics at individual particles in complex colloidal systems. *J. Phys. Chem. C* **123**, 21639–21644 (2019).

46. Q. Liu, A. Prosperetti, Wall effects on a rotating sphere. *J. Fluid Mech.* **657**, 1–21 (2010).

47. A. J. Goldman, R. G. Cox, H. Brenner, Slow viscous motion of a sphere parallel to a plane wall—I motion through a quiescent fluid. *Chem. Eng. Sci.* **22**, 637–651 (1967).

48. A. P. Bregulla, A. Wurger, K. Gunther, M. Mertig, F. Cichos, Thermo-osmotic flow in thin films. *Phys. Rev. Lett.* **116**, 188303 (2016).

49. J. Gargiulo, T. Brick, I. L. Violi, F. C. Herrera, T. Shibanuma, P. Albella, F. G. Requejo, E. Cortés, S. A. Maier, F. D. Stefani, Understanding and reducing photothermal forces for the fabrication of au nanoparticle dimers by optical printing. *Nano Lett.* **17**, 5747–5755 (2017).

50. M. Heidari, A. Bregulla, S. Muinos Landin, F. Cichos, R. von Klitzing, Self-propulsion of Janus particles near a brush-functionalized substrate. *Langmuir* **36**, 7775–7780 (2020).

51. A. Majee, A. Würger, Thermocharge of a hot spot in an electrolyte solution. *Soft Matter* **9**, 2145–2153 (2013).

52. S. A. Putnam, D. G. Cahill, Transport of nanoscale latex spheres in a temperature gradient. *Langmuir* **21**, 5317–5323 (2005).

53. A. Wurger, Transport in charged colloids driven by thermoelectricity. *Phys. Rev. Lett.* **101**, 108302 (2008).

54. L. Lin, X. Peng, X. Wei, Z. Mao, C. Xie, Y. Zheng, Thermophoretic tweezers for low-power and versatile manipulation of biological cells. *ACS Nano* **11**, 3147–3154 (2017).

55. L. Ninni, H. Burd, W. H. Fung, A. J. A. Meirelles, Kinematic viscosities of poly(ethylene glycol) aqueous solutions. *J. Chem. Eng. Data* **48**, 324–329 (2003).

56. K. Ohsawa, M. Murata, H. Ohshima, Zeta potential and surface charge density of polystyrene-latex; comparison with synaptic vesicle and brush border membrane vesicle. *Colloid Polym. Sci.* **264**, 1005–1009 (1986).

57. S. Zhu, U. Panne, K. Rurack, A rapid method for the assessment of the surface group density of carboxylic acid-functionalized polystyrene microparticles. *Analyst* **138**, 2924–2930 (2013).

58. E. Lee, D. Huang, T. Luo, Ballistic supercavitating nanoparticles driven by single Gaussian beam optical pushing and pulling forces. *Nat. Commun.* **11**, 2404 (2020).

59. L. Lin, X. Peng, Z. Mao, W. Li, M. N. Yogeesh, B. B. Rajeeva, E. P. Perillo, A. K. Dunn, D. Akinwande, Y. Zheng, Bubble-pen lithography. *Nano Lett.* **16**, 701–708 (2016).

60. C. Zhao, Y. Xie, Z. Mao, Y. Zhao, J. Rufo, S. Yang, F. Guo, J. D. Mai, T. J. Huang, Theory and experiment on particle trapping and manipulation via optothermally generated bubbles. *Lab Chip* **14**, 384–391 (2014).

61. M. Sitti, D. S. Wiersma, Pros and cons: Magnetic versus optical microrobots. *Adv. Mater.* **32**, e1906766 (2020).

62. V. A. Singh, M. Sitti, Targeted drug delivery and imaging using mobile milli/microrobots: A promising future towards theranostic pharmaceutical design. *Curr. Pharm. Des.* **22**, 1418–1428 (2016).

63. J. Li, E. H. Hill, L. Lin, Y. Zheng, Optical nanoprinting of colloidal particles and functional structures. *ACS Nano* **13**, 3783–3795 (2019).

64. S. M. Tazhibaeva, K. B. Musabekov, A. B. Orazymbetova, A. A. Zhubanova, Surface properties of yeast cells. *Colloid J.* **65**, 122–124 (2003).

65. Y. Fu, P. W. Winter, R. Rojas, V. Wang, M. McAuliffe, G. H. Patterson, Axial superresolution via multiangle TIRF microscopy with sequential imaging and photobleaching. *Proc. Natl. Acad. Sci. U.S.A.* **113**, 4368–4373 (2016).

66. R. Bharadwaj, V. V. R. Sai, K. Thakare, A. Dhawangale, T. Kundu, S. Titus, P. K. Verma, S. Mukherji, Evanescent wave absorbance based fiber optic biosensor for label-free detection of *E. coli* at 280 nm wavelength. *Biosens. Bioelectron.* **26**, 3367–3370 (2011).

67. C. R. Taitt, G. P. Anderson, F. S. Ligler, Evanescent wave fluorescence biosensors: Advances of the last decade. *Biosens. Bioelectron.* **76**, 103–112 (2016).

68. K. N. Fish, Total internal reflection fluorescence (TIRF) microscopy. *Curr. Protoc. Cytom.* Chapter 12, Unit12.18 (2009).

69. K. He, R. Marsland III, S. Upadhyayula, E. Song, S. Dang, B. R. Capraro, W. Wang, W. Skillern, R. Gaudin, M. Ma, T. Kirchhausen, Dynamics of phosphoinositide conversion in clathrin-mediated endocytic traffic. *Nature* **552**, 410–414 (2017).

70. S. S. Li, C. K. M. Ip, M. Y. H. Tang, M. K. S. Tang, Y. Tong, J. Zhang, A. A. Hassan, A. S. C. Mak, S. Yung, T. M. Chan, P. P. Ip, C. L. Lee, P. C. N. Chiu, L. T. O. Lee, H. C. Lai, J. Z. Zeng, H. C. Shum, A. S. T. Wong, Sialyl Lewisx-P-selectin cascade mediates tumor-mesothelial adhesion in ascitic fluid shear flow. *Nat. Commun.* **10**, 2406 (2019).

71. M. Pruenster, A. R. M. Kurz, K. J. Chung, X. Cao-Ehlker, S. Bieber, C. F. Nussbaum, S. Bierschenk, T. K. Eggersmann, I. Rohwedder, K. Heinig, R. Immler, M. Moser, U. Koedel, S. Gran, R. P. McEver, D. Vestweber, A. Verschoor, T. Leanderson, T. Chavakis, J. Roth, T. Vogl, M. Sperandio, Extracellular MRP8/14 is a regulator of β2 integrin-dependent neutrophil slow rolling and adhesion. *Nat. Commun.* **6**, 6915 (2015).

72. H. Ceylan, I. C. Yasa, U. Kilic, W. Hu, M. Sitti, Translational prospects of untethered medical microrobots. *Prog. Biomed. Eng.* **1**, 012002 (2019).

73. J. Zhou, Y. Jiang, S. Hou, P. K. Upputuri, D. Wu, J. Li, P. Wang, X. Zhen, M. Pramanik, K. Pu, H. Duan, Compact plasmonic blackbody for cancer theranosis in the near-infrared II window. *ACS Nano* **12**, 2643–2651 (2018).

74. H. J. C. Berendsen, J. R. Grigera, T. P. Straatsma, The missing term in effective pair potentials. *J. Phys. Chem.* **91**, 6269–6271 (1987).

75. H. Ding, G. Peng, S. Mo, D. Ma, S. W. Sharshir, N. Yang, Ultra-fast vapor generation by a graphene nano-ratchet: A theoretical and simulation study. *Nanoscale* **9**, 19066–19072 (2017).

76. W. D. Cornell, P. Cieplak, C. I. Bayly, I. R. Gould, K. M. Merz, D. M. Ferguson, D. C. Spellmeyer, T. Fox, J. W. Caldwell, P. A. Kollman, A second generation force field for the simulation of proteins, nucleic acids, and organic molecules. *J. Am. Chem. Soc.* **117**, 5179–5197 (1995).

77. X. Sui, H. Ding, Z. Yuan, C. F. Leong, K. Goh, W. Li, N. Yang, D. M. D'Alessandro, Y. Chen, The roles of metal-organic frameworks in modulating water permeability of graphene oxide-based carbon membranes. *Carbon* **148**, 277–289 (2019).

78. M. Mohsen-Nia, H. Modarress, H. Rasa, Measurement and modeling of density, kinematic viscosity, and refractive index for poly(ethylene glycol) aqueous solution at different temperatures. *J. Chem. Eng. Data* **50**, 1662–1666 (2005).

79. P. B. Johnson, R. W. Christy, Optical constants of the noble metals. *Phys. Rev. B* **6**, 4370–4379 (1972).